ACS APPLIED MATERIALS & INTERFACES

Research Article

www.acsami.org

Composition-Dependent Electrocatalytic Activity of Palladium–Iridium Binary Alloy Nanoparticles Supported on the Multiwalled Carbon Nanotubes for the Electro-Oxidation of Formic Acid

Jianming Bao, Meiling Dou, Haijing Liu,* Feng Wang,* Jingjun Liu, Zhilin Li, and Jing Ji

State Key Laboratory of Chemical Resource Engineering, Beijing Key Laboratory of Electrochemical Process and Technology for Materials, Beijing University of Chemical Technology, Beijing 100029, P. R. China

ABSTRACT: Surface-functionalized multiwalled carbon nanotubes (MWCNTs) supported $Pd_{100-x}Ir_x$ binary alloy nanoparticles ($Pd_{100-x}Ir_x$/MWCNT) with tunable Pd/Ir atomic ratios were synthesized by a thermolytic process at varied ratios of bis(acetylacetonate) palladium(II) and iridium-(III) 2,4-pentanedionate precursors and then applied as the electrocatalyst for the formic acid electro-oxidation. The X-ray diffraction pattern (XRD) and transmission electron microscope (TEM) analysis showed that the $Pd_{100-x}Ir_x$ alloy nanoparticles with the average size of 6.2 nm were uniformly dispersed on the MWCNTs and exhibited a single solid solution phase with a face-centered cubic structure. The electrocatalytic properties were evaluated through the cyclic voltammetry and chronoamperometry tests, and the results indicated that both the activity and stability of $Pd_{100-x}Ir_x$/MWCNT were strongly dependent on the Pd/Ir atomic ratios: the best electrocatalytic performance in terms of onset potential, current density, and stability against CO poisoning was obtained for the $Pd_{79}Ir_{21}$/MWCNT. Moreover, compared with pure Pd nanoparticles supported on MWCNTs (Pd/MWCNT), the $Pd_{79}Ir_{21}$/MWCNT exhibited enhanced steady-state current density and higher stability, as well as maintained excellent electrocatalytic activity in high concentrated formic acid solution, which was attributed to the bifunctional effect through alloying Pd with transition metal.

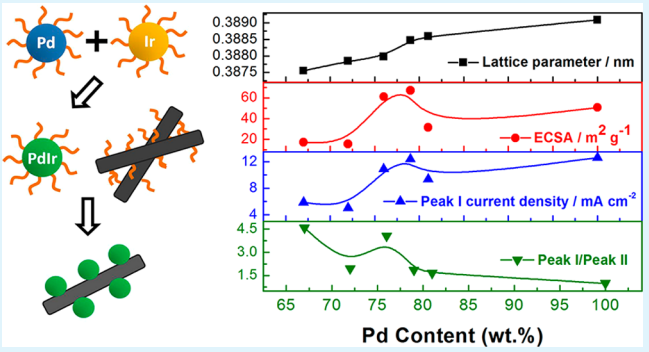

KEYWORDS: *formic acid electro-oxidation, palladium iridium alloy, bifunctional effect, composition-dependent, stability*

1. INTRODUCTION

During the past decade, the direct formic acid fuel cell (DFAFC) has attracted much attention due to its high theoretical open-circuit voltage (1.48 V) and enhanced proton transport in the electrocatalyst layer.[1−4] Compared with the usage of methanol in the direct methanol fuel cell (DMFC) system, the main advantage of applying formic acid as the fuel in the DFAFC system is the lower fuel crossover through the polymer membrane.[4] As a result, the optimal operating concentration might be increased as high as ∼20 mol L^{-1}, thus significantly improving the power density and the energy conversion efficiency. Furthermore, the formic acid can be easily handled during the storage and transportation process because it is nontoxic and inflammable at room temperature.[5]

Although formic acid is considered as a promising alternative to methanol in fuel cells, there are still several obstacles hindering the commercialization of DFAFC. One of the main challenges is that the anode platinum (Pt), which is currently considered the best electrocatalyst, tends to be easily poisoned by intermediates formed during the incomplete oxidation process of the formic acid.[6] When applying Pt as the electrocatalyst, the formic acid mainly occurs via a dual-pathway mechanism: the adsorbed formate ion produced through dehydrogenation reaction (direct pathway) is identified as the reactive intermediate, while the strongly adsorbed CO (CO_{ads}) produced through the dehydration reaction (indirect pathway) is identified as the poisonous intermediate.[7,8] The formation of CO_{ads} leads to the self-poisoning of Pt electrocatalysts,[9−11] and the elimination of CO_{ads} is difficult unless applying a higher potential than that of operating conditions in DFAFC.[12]

As a potential alternative to the Pt electrocatalyst, Pd that is almost half the price is believed to promote the formic acid oxidation (FAO) through the direct pathway with less CO_{ads}, thus is less vulnerable to CO_{ads} poisoning,[8,13−15] but it undergoes the deactivation during the FAO process.[16−19] To further improve the electrocatalytic performances of Pd, alloying with transition metal species[16,19,20] is one of the most effective methods due to the bifunctional mechanism, as the secondary metal has been proved to promote the dissociation of water to form adsorbed OH, which can oxidize CO_{ads} to CO_2.[9,21,22] Among the various alternatives introduced in the alloy electrocatalysts, Ir is also reported as a superior secondary transition-metal component to enhance the catalytic

Received: March 1, 2015
Accepted: July 1, 2015
Published: July 1, 2015

DOI: 10.1021/acsami.5b01848
ACS Appl. Mater. Interfaces 2015, 7, 15223−15229

properties[23] because the oxygen species can be formed on the surface of Ir at relatively low potentials.[24] Shen et al.[25] synthesized carbon-supported bimetallic PdIr catalysts with different atomic ratios through a simple NaBH-reduction method. When applied for the ethanol oxidation, Pd_7Ir/C exhibited the highest activity and stability. Assumpcao et al.[26] also proved that the enhanced catalytic activity could be achieved with carbon-supported PdIr alloy nanoparticle catalysts in the case of ammonia oxidation in alkaline solutions. On the basis of the previous research works, the superior catalytic properties of PdIr alloy nanoparticle catalysts may be expended to the FAO process. As the catalytic properties of alloy nanoparticles are greatly influenced by the particle dimensions and compositions,[5,27,28] further studies on optimizing the ratio of metal components to maximize the FAO catalytic activity are essential. However, former studies mainly focused on the compositional effect on the catalytic activities of bulk electrode, as accurately controlling the composition of nanoparticles is quite difficult.[6] Therefore, evaluating the influence of Pd/Ir ratio within the nanoscales on the catalytic properties for the FAO process is still a demanding task.

In this study, the novel surface-functionalized multiwalled carbon nanotubes (MWCNTs) supported $Pd_{100-x}Ir_x$ alloy nanoparticles ($Pd_{100-x}Ir_x$/MWCNT) with different metal ratios were prepared and applied as the electrocatalyst for the FAO. The compositions were estimated by the energy-dispersive X-ray detector (EDS) analysis and confirmed by the X-ray diffraction (XRD), together with X-ray photoelectron spectroscopy (XPS) results. By evaluating the catalytic activity for the FAO process and stability against CO_{ads} within the present experimental contents, it was found that $Pd_{79}Ir_{21}$/MWCNT exhibited dramatically enhanced electrocatalytic performances among the various alloy nanoparticles when compared with pure Pd nanoparticles supported on surface-functionalized MWCNTs (Pd/MWCNT).

2. EXPERIMENTAL SECTION

2.1. Materials. Bis(acetylacetonate) palladium(II) ($Pd(acac)_2$, 99%, J&K scientific Ltd.), iridium(III) 2,4-pentanedionate ($Ir(acac)_3$, Ir 37.5%, Alfa Aesar), tri-*n*-octylphosphine (TOP, 90%, Alfa Aesar), oleylamine (90%, J&K scientific Ltd.), Nafion solution (5 wt %, DuPont USA), and MWCNTs (SHOWA DENKO) were used. Ethanol, hexane, toluene, formic acid (HCOOH), and perchloric acid ($HClO_4$) were purchased from Sinopharm Chemical Reagent Ltd. without further treatment.

2.2. Synthesis of $Pd_{100-x}Ir_x$/MWCNT. $Pd_{100-x}Ir_x$/MWCNTs (x = 33, 28, 24, 21, and 19) were synthesized through the following steps: $Pd(acac)_2$ (0.188 mmol L^{-1}) and $Ir(acac)_3$ (0.094−0.047 mmol L^{-1}) were dissolved in 1 mL of TOP by sonication and bubbled with high purity N_2 for 30 min. The solution was injected into 3 mL of 300 °C oleylamine under N_2 flow and kept at 300 °C for an hour. After cooling to room temperature, 5 mL of hexane and 30 mL of ethanol were added, and the resulting nanoparticles were collected by centrifugation. MWCNTs applied as the support material were first surface functionalized under refluxing in 200 mL of 120 °C and 14 mol L^{-1} HNO_3 for 10 h, in order to create surface oxygen-containing functional groups, which are highly favored for anchoring nanoparticles. The powder was collected on a 250 nm pore membrane filter and rinsed with ultrapure water several times. Then, 50 mg of surface-functionalized MWCNTs were sonicated in 150 mL of toluene containing 0.25 mL of oleylamine for 4 h, followed by separation from the solution by centrifugation. The oleylamine-stabilized nanoparticles and MWCNTs were dispersed in 100 mL of hexane and then evaporated at 80 °C in air. Finally, the oleylamine and TOP were removed by low-temperature thermal annealing at 200 °C for 3 h in air. For comparison, Pd nanoparticles loaded on MWCNTs were prepared using the same method.

2.3. Catalyst Characterization. The morphology of $Pd_{100-x}Ir_x$/MWCNT was investigated by a transmission electron microscope (TEM, JEOL JEM-2100) operated at 200 kV. EDS (OXFORD instruments) was carried out to evaluate the nanoparticle compositions. Powder XRD measurement was carried out on a Rigaku D/max-2500 with Cu Kα (α = 1.54 Å). XPS (Thermo Fisher Scientific ESCALAB 250) was performed to analyze the surface characteristics of the electrocatalysts.

2.4. Electrochemical Measurement. Electrochemical measurements were carried out using a conventional three-electrode cell at room temperature with an AUTOLAB PGSTAT302N electrochemical workstation. The counter electrode was Pt foil, and a saturated calomel electrode (SCE) was used as reference electrode. The working electrode was prepared by the following procedure. Briefly, 4 mg of electrocatalysts was mixed with 0.9 mL of ethanol and 0.1 mL of nafion solution (5 wt %, DuPont USA) to form electrocatalyst ink by ultrasonication. Then 10 μL of the ink was casted onto a glassy carbon electrode (0.071 cm^2 geometrical area). The electrolyte was 0.1 mol L^{-1} HCOOH and 0.1 mol L^{-1} $HClO_4$ solution and bubbled with N_2 for 30 min before the tests. All the current densities were normalized to the geometric surface area of the electrode.

3. RESULTS AND DISCUSSION

The composition of the $Pd_{100-x}Ir_x$ nanoparticles was estimated by the EDS analysis, and the atomic ratios were determined to be $Pd_{67}Ir_{33}$, $Pd_{72}Ir_{28}$, $Pd_{76}Ir_{24}$, $Pd_{79}Ir_{21}$, and $Pd_{81}Ir_{19}$. Figure 1

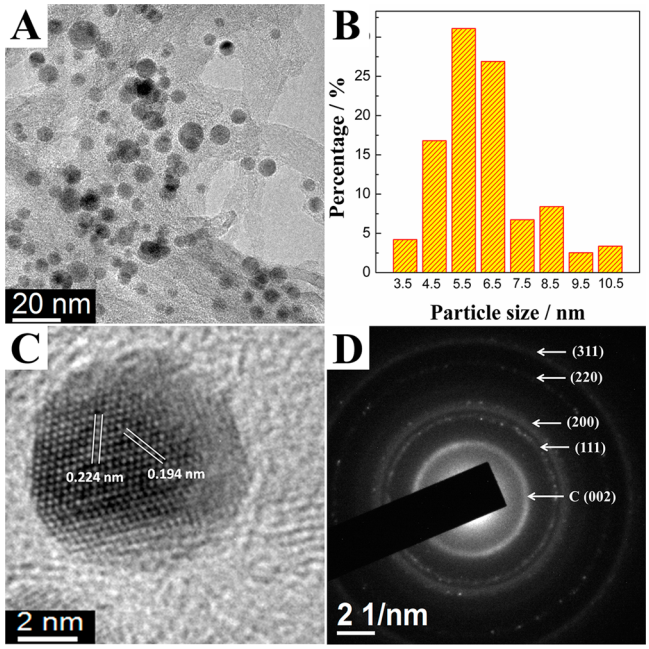

Figure 1. (A),(C) HR-TEM images of PdIr/MWCNT with different resolutions, (B) the particle size distributions, and (D) the selected area diffraction pattern.

exhibits the typical HR-TEM images of PdIr/MWCNT ($Pd_{79}Ir_{21}$/MWCNT), the corresponding particle size distribution histogram and selected area electron diffraction (SAED) pattern. As presented in Figure 1A, the nanoparticles ranging from 3.7 to 12.5 nm are well dispersed on the surface-functionalized MWCNTs with an average diameter of 6.2 nm, and the well-defined crystalline lattice fringes obtained from the SAED pattern reveal polycrystalline face centered cubic (fcc) structures of the nanoparticles. The HR-TEM image for a single

DOI: 10.1021/acsami.5b01848
ACS Appl. Mater. Interfaces 2015, 7, 15223−15229

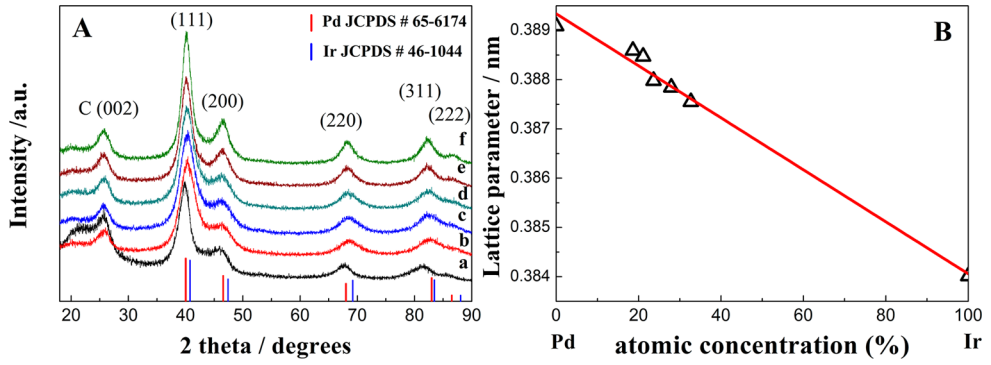

Figure 2. (A) XRD patterns of (a) Pd/MWCNT, (b) $Pd_{67}Ir_{33}$/MWCNT, (c) $Pd_{72}Ir_{28}$/MWCNT, (d) $Pd_{76}Ir_{24}$/MWCNT, (e) $Pd_{79}Ir_{21}$/MWCNT, and (f) $Pd_{81}Ir_{19}$/MWCNT. (B) The plot of lattice parameter versus Ir concentration.

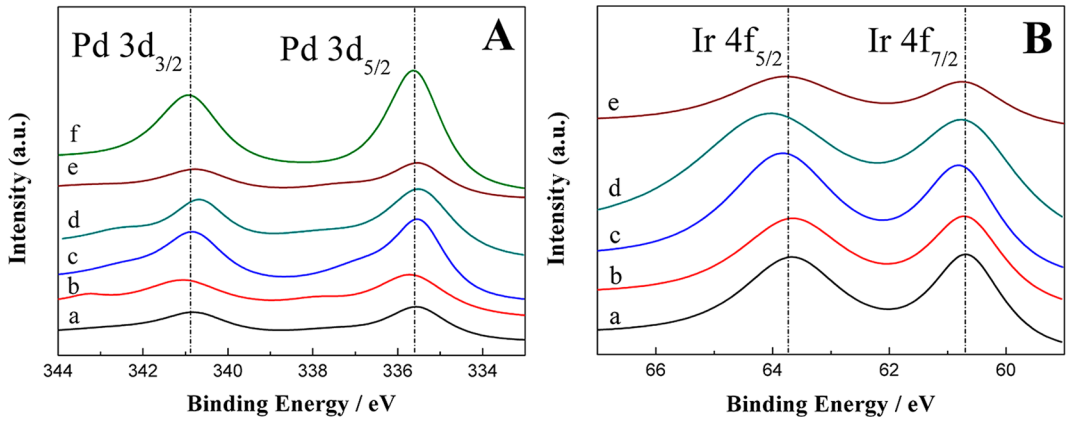

Figure 3. XPS spectra of the (A) Pd 3d and (B) Ir 4f regions of (a) $Pd_{67}Ir_{33}$/MWCNT, (b) $Pd_{72}Ir_{28}$/MWCNT, (c) $Pd_{76}Ir_{24}$/MWCNT, (d) $Pd_{79}Ir_{21}$/MWCNT, (e) $Pd_{81}Ir_{19}$Ir/MWCNT, and (f) Pd/MWCNT.

nanoparticle exhibits interplanar spacing of 0.225 and 0.195 nm, which is slightly larger than the standard value of Pd(111) and (200) planes (0.224 and 0.194 nm, JCPDS No. 65-6174), respectively, indicating that Ir atoms probably incorporated into the Pd lattice and substituted Pd atoms to form a single PdIr solid solution within the whole atomic ratios.

The XRD patterns of Pd/MWCNT and $Pd_{100-x}Ir_x$/MWCNT with different atomic ratios are presented in Figure 2. The broad diffraction peak centered at ~25.6° is assigned to the hexagonal structure (002) plane of MWCNTs, and other peaks at 39.74°, 46.22°, 67.60°, 81.46°, and 85.75° are attributed to Pd(111), (200), (220), (311), and (222) planes with fcc crystalline structure (JCPDS-ICDD, card No. 04-802). The diffraction peaks of $Pd_{100-x}Ir_x$/MWCNT alloy catalysts are located at higher 2θ values with respect to those of Pd/MWCNT, demonstrating that the lattice contraction was caused by the incorporation of a lower d space crystal structure of Ir (d_{111} = 2.217) compared with Pd (d_{111} = 2.246).[29,30] Furthermore, no diffraction peaks related to Ir or Ir oxide can be observed, further proving that Ir atoms have inserted into the Pd lattice to form the alloy. In order to better understand the alloy structure of $Pd_{100-x}Ir_x$/MWCNT, the lattice parameter of $Pd_{100-x}Ir_x$ with different atomic ratios was calculated from the (111) crystalline plane applying the following formula[15]

$$a = \sqrt{3}\lambda/\sin\theta$$

where a is the lattice parameter; λ is the wavelength of the X-ray; and θ is the angle of the maximum peak. As exhibited in Figure 2B, a linear relation exists between the lattice parameter and the atomic concentration of Ir, which indicates that the $Pd_{100-x}Ir_x$ alloy formed a single solid solution phase according to the Vegard's Law.[31] The crystalline size of $Pd_{79}Ir_{21}$ nanoparticles estimated by Scherrer's equation[32] from the (220) plane is 5.7 nm, which is slightly smaller than the TEM result (6.2 nm).

XPS measurements were performed to determine the surface chemical states of the alloy nanoparticles. As shown in Figure 3, the peaks centered at ~335.6 and 340.8 eV are assigned to the Pd $3d_{5/2}$ and Pd $3d_{3/2}$ core electrons, which are in good agreement with the previous report.[33] The peaks at 60.7 and 63.7 eV in Figure 3(B) are attributed to the doublets of Ir $4f_{7/2}$ and Ir $4f_{5/2}$, which correspond to metallic Ir.[31] For $Pd_{76}Ir_{24}$/MWCNT, $Pd_{79}Ir_{21}$/MWCNT, and $Pd_{81}Ir_{19}$/MWCNT, the peaks for Pd $3d_{5/2}$ and Pd $3d_{3/2}$ shift to lower binding energies compared with Pd/MWCNT. On the contrary, the binding energies of Ir $4f_{7/2}$ and Ir $4f_{5/2}$ exhibit a simultaneous increase. The shifts of the binding energies might be attributed to the electronic interactions between the Pd and Ir atomic orbital, leading to electron transfer from Ir to Pd.[5] However, such binding energy shifts are not observed in $Pd_{67}Ir_{33}$/MWCNT and $Pd_{72}Ir_{28}$/MWCNT.

Before analyzing the catalytic properties for the FAO, the electrochemical active surface areas (ECSAs) of the electrocatalysts were evaluated by the CO stripping voltammetry tests, in which CO was adsorbed onto the electrode at −0.15 V by bubbling the gas through the 0.5 mol L^{-1} $HClO_4$ solution for 30 min. Dissolved CO was subsequently removed while

DOI: 10.1021/acsami.5b01848
ACS Appl. Mater. Interfaces 2015, 7, 15223−15229

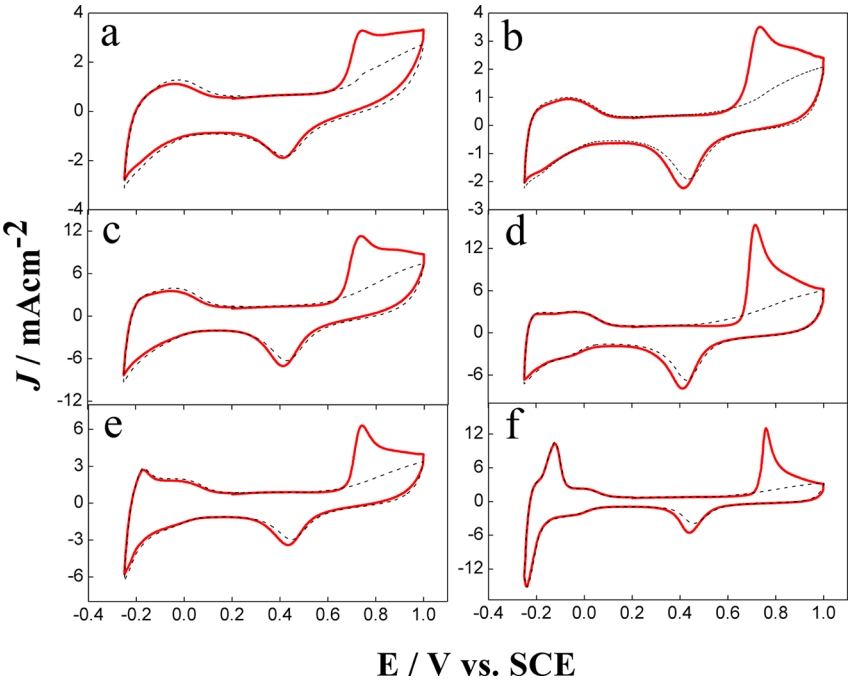

Figure 4. CO stripping voltammograms on (a) $Pd_{67}Ir_{33}$/MWCNT, (b) $Pd_{72}Ir_{28}$/MWCNT, (c) $Pd_{76}Ir_{24}$/MWCNT, (d) $Pd_{79}Ir_{21}$/MWCNT, (e) $Pd_{81}Ir_{19}$/MWCNT, and (f) Pd/MWCNT at a scan rate of 25 mV s^{-1} in 0.5 mol L^{-1} $HClO_4$ solution.

Table 1. Electrochemical Parameters of Different Electrocatalysts

electrocatalyst	ECSA (m^2 g^{-1})	onset potential of CO oxidation (V vs SCE)	peak potential of CO oxidation (V vs SCE)	peak I current density (mA cm^{-2})	peak II current density (mA cm^{-2})
$Pd_{67}Ir_{33}$/MWCNT	17.30	0.61	0.73	5.87	1.28
$Pd_{72}Ir_{28}$/MWCNT	15.64	0.61	0.74	5.03	2.58
$Pd_{76}Ir_{24}$/MWCNT	61.16	0.63	0.73	10.88	2.68
$Pd_{79}Ir_{21}$/MWCNT	67.15	0.62	0.71	12.38	6.69
$Pd_{81}Ir_{19}$/MWCNT	31.52	0.66	0.74	9.35	5.64
Pd/MWCNT	50.71	0.71	0.76	12.60	12.70

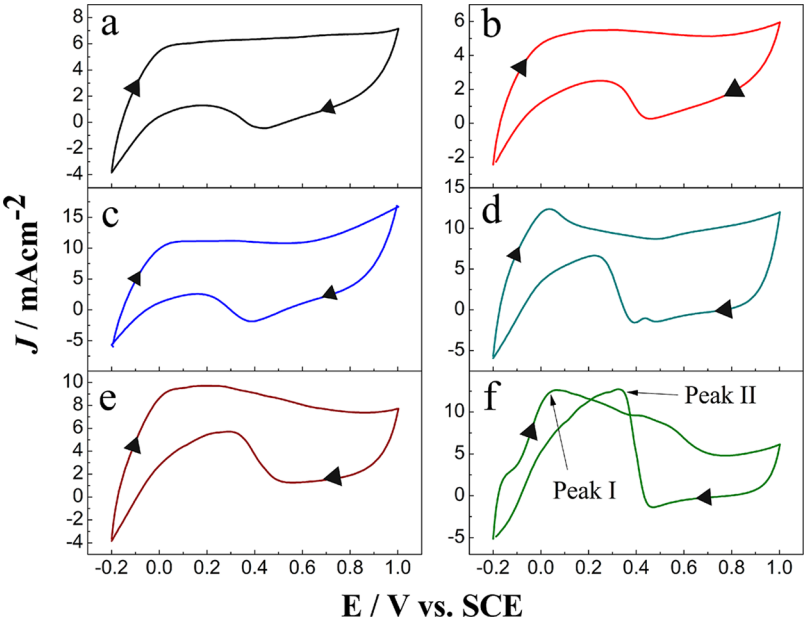

Figure 5. Cyclic voltammograms on (a) $Pd_{67}Ir_{33}$/MWCNT, (b) $Pd_{72}Ir_{28}$/MWCNT, (c) $Pd_{76}Ir_{24}$/MWCNT, (d) $Pd_{79}Ir_{21}$/MWCNT, (e) $Pd_{81}Ir_{19}$/MWCNT, and (f) Pd/MWCNT at a scan rate of 50 mV s^{-1} in 0.1 mol L^{-1} $HClO_4$ solution with 0.1 mol L^{-1} HCOOH.

DOI: 10.1021/acsami.5b01848
ACS Appl. Mater. Interfaces 2015, 7, 15223−15229

maintaining the potential at −0.15 V. As shown in Figure 4, CV curves were recorded from −0.25 to 1.0 V at a sweep rate of 25 mV s^{-1}. The ECSA was determined according to the following formula[34]

$$\mathrm{ECSA} = \frac{Q_{\mathrm{CO}}}{[\mathrm{Pd}] \times 0.42}$$

where Q_{CO} is the stripping charge of CO adsorption (mC/cm^{-2}); [Pd] represents the Pd loading (mg cm^{-2}); and 0.42 represents the charge required to oxidize a monolayer of adsorbed CO. According to the results, the ECSA obtained for $Pd_{79}Ir_{21}$/MWCNT (67.15 m^2 g^{-1}) is larger than the other MWCNT-supported alloy nanoparticles and Pd/MWCNT (50.71 m^{-2} g^{-1}). Furthermore, the onset and peak potential of CO_{ads} oxidation on the $Pd_{100-x}Ir_x$/MWCNT negatively shift compared with Pd/MWCNT (as shown in Table 1), indicating that the incorporated Ir atoms may facilitate the decomposition of water to form adsorbed OH species, which then oxidize CO_{ads} to CO_2 on Pd sites to remove the poisoning intermediate.[5,35,36]

Figure 5 exhibits the steady-state CV curves of the catalysts with different elemental ratios for the FAO process. As evidenced by the literature,[8,37] an anodic peak appears at ~0.07 V (Peak I) which corresponds to the oxidation of formic acid through the direct pathway, which is directly oxidized to CO_2. No poisoning intermediate is formed, while another peak located at ~0.41 V (Peak II) can be mainly attributed to the indirect pathway. Observed from Figure 5, we can find that Pd/MWCNT and $Pd_{79}Ir_{21}$/MWCNT exhibit two major voltammetric peaks, indicating the direct pathway of FAO occurred on the surface of these two electrocatalysts, whereas only one peak at the backward scans can be observed for the other MWCNT-supported alloy nanoparticle electrocatalysts, which suggested that the FAO process might proceed through the dual pathway. Obviously, the dual pathway is not favored for the effective electro-oxidation of the formic acid.[8] Compared with Pd/MWCNT, the Peak I potentials of $Pd_{79}Ir_{21}$/MWCNT shift ~50 mV to the lower values. By comparing the current density at the potential where Peak I lies among the electrocatalysts, the largest value was observed with the $Pd_{79}Ir_{21}$/MWCNT (shown in Table 1). As Ir has no electrocatalytic activity toward the FAO,[23] the enhancement might be attributed to the modification in the surface electronic structure of $Pd_{100-x}Ir_x$ alloy nanoparticles, leading to optimal adsorbate−metal bond strength between formic acid and Pd.[38] Furthermore, the $Pd_{79}Ir_{21}$/MWCNT exhibits comparable catalytic properties compared with other Pd-base alloy electrocatalysts.[39−41]

The ratio of Peak I to Peak II current densities is an indication of the direct pathway relative to the indirect pathway, which suggests the stability against CO poisoning.[42] When comparing Pd/MWCNT and $Pd_{79}Ir_{21}$/MWCNT, the corresponding Peak I/Peak II current ratios are found to be 0.99 and 1.85, respectively, indicating that the indirect pathway for FAO on $Pd_{79}Ir_{21}$/MWCNT is significantly suppressed. Similar to the Pt-based electrocatalysts, the mechanism of suppression for indirect pathway and the facilitation for direct pathway[43] on the $Pd_{100-x}Ir_x$ alloy nanoparticles might be described as follows: As the CO_{ads} formation via an indirect pathway requires at least three adjacent precious metal atoms, the introduction of Ir atoms formed noncontinuous Pd sites on the surface, thus highly favoring the direct pathway process for the FAO and inhibiting CO_{ads} poisoning.

As described above, the operating concentration can be significantly increased when applying formic acid as the fuel. However, higher formic acid concentration might cause positive shifts of the peak potentials for the FAO due to the CO_{ads} poisoning. In order to evaluate the stability of PtIr alloy electrocatalysts against various formic acid concentrations, linear polarization curves are observed in different solutions (Figure 6). As the concentration of formic acid increased from

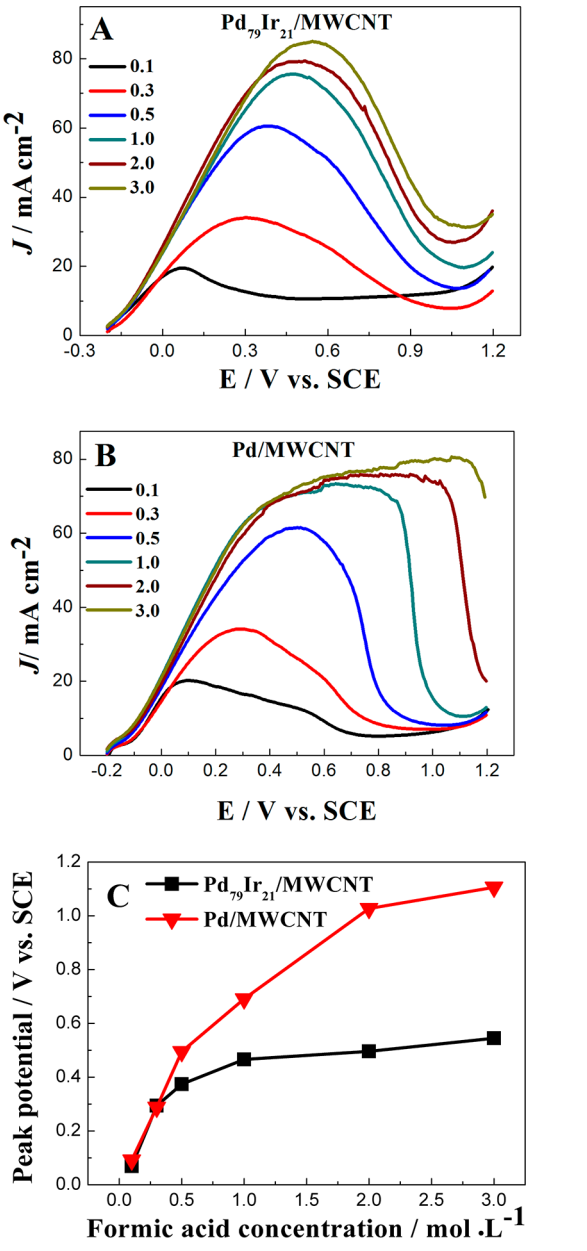

Figure 6. Linear polarization curves of (A) $Pd_{79}Ir_{21}$/MWCNT and (B) Pd/MWCNT at a scan rate of 50 mV s^{-1} with the formic acid concentration increased from 0.1 to 3.0 mol L^{-1} and (C) the plot of peak potentials versus formic acid concentrations.

1.0 to 3.0 mol L^{-1}, the FAO peak potentials of Pd/MWCNT shift from 0.09 to 1.11 V, while only 0.47 V shifts from 0.07 to 0.54 V can be observed with the $Pd_{79}Ir_{21}$/MWCNT. The results indicate that $Pd_{79}Ir_{21}$/MWCNT is less sensitive to CO_{ads} poisoning, thus keeping excellent electrocatalytic activity in high concentrated formic acid solutions.

DOI: 10.1021/acsami.5b01848
ACS Appl. Mater. Interfaces 2015, 7, 15223−15229

The long-term stability of the $Pd_{100-x}Ir_x$/MWCNT was evaluated by the chronoamperometry tests carried out in 0.1 mol L^{-1} $HClO_4$ solutions with 0.1 mol L^{-1} HCOOH at fixed potential of 0.05 V (Figure 7A). The initial high currents are

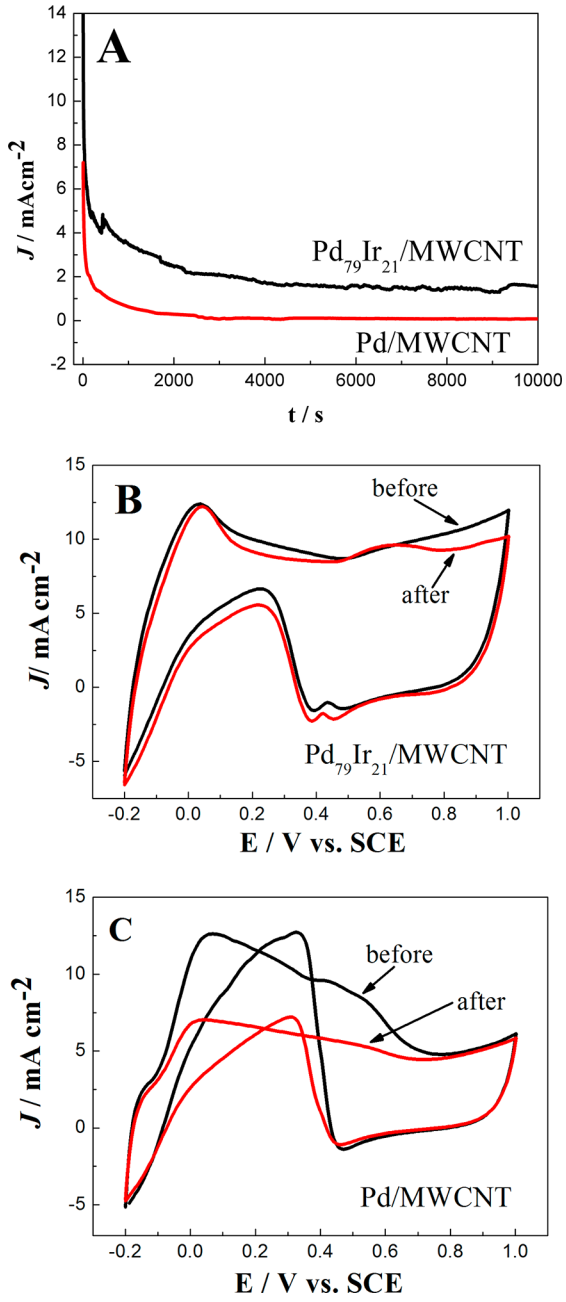

Figure 7. (A) Chronoamperometric curves of $Pd_{79}Ir_{21}$/MWCNT and Pd/MWCNT at 0.05 V vs SCE in 0.1 mol L^{-1} $HClO_4$ solutions with 0.1 mol L^{-1} HCOOH. Cyclic voltammograms before and after the stability test on (B) $Pd_{79}Ir_{21}$/MWCNT and (C) Pd/MWCNT.

caused by the combination of double-layer charging and formic acid oxidation. The current quickly decayed due to the adsorption of poisoning intermediates and reached steady state after a few seconds, while the initial current density on the $Pd_{79}Ir_{21}$/MWCNT decreased much more slowly than the Pd/MWCNT, which is attributed to the higher ECSA and less CO_{ads} poisoning.[30] By comparing the current densities at 10 000 s, the $Pd_{79}Ir_{21}$/MWCNT exhibits much larger value (1.56 mA cm^{-2}) than the Pd/MWCNT (0.08 mA cm^{-2}), which clearly presents the superior activity of the alloy electrocatalysts. Furthermore, the CV curves before and after the stability test were also recorded. As shown in Figure 7(B) and (C), only a slight decrease in the Peak I current density of $Pd_{79}Ir_{21}$/MWCNT could be observed after the stability test, while the current density of Pd/MWCNT significantly decreased from 12.60 to 7.04 mA cm^{-2}. These results further confirm the enhanced electrocatalytic activity and stability of $Pd_{79}Ir_{21}$/MWCNT, suggesting that it is a promising anode electrocatalyst for the DFAFC.

4. CONCLUSIONS

In summary, PdIr alloy nanoparticles with controllable atomic ratios were successfully synthesized and supported on the MWCNTs through an oleylamine-mediated method. As observed from the HR-TEM images, the $Pd_{100-x}Ir_x$ alloy nanoparticles were well dispersed on the surface of the MWCNTs with an average diameter of 6.2 nm. Within the whole atomic ratios, the alloy particles formed a single solid solution with Ir atoms inserted into the lattice of Pd, disorganizing the atomic arrangement to decrease the surface adsorption of poisoning intermediates during the electrocatalytic process. When applied for the electrocatalysts toward the FAO process, it was found that the alloy compositions of $Pd_{100-x}Ir_x$/MWCNT significantly influence the catalytic performance. Among the samples with controlled atomic ratios, the $Pd_{79}Ir_{21}$/MWCNT exhibits the best electrocatalytic properties, with higher catalytic current density and stability against CO_{ads} poisoning. Compared with Pd/MWCNT, the $Pd_{79}Ir_{21}$/MWCNT is less sensitive to the concentration of formic acid in the electrolyte, maintaining its excellent activity even in 3 mol L^{-1} solutions. Furthermore, the alloy nanoparticle electrocatalysts also exhibited enhanced steady-state current density and long-term stability evaluated from the stability test. On the basis of the results, it can be concluded that the compositional effect of alloy nanoparticles highly influences the catalytic properties for the FAO process, and $Pd_{100-x}Ir_x$/MWCNT with certain atomic ratio might be developed as a promising anode electrocatalyst for the DFAFC.

AUTHOR INFORMATION

Corresponding Authors

*Dr. H. Liu. E-mail: 2010080070@grad.buct.edu.cn.
*Prof. F. Wang. E-mail: wangf@mail.buct.edu.cn.

Notes

The authors declare no competing financial interest.

ACKNOWLEDGMENTS

This work was supported by National Natural Science Funds of China (51125007)

REFERENCES

(1) Yu, X.; Pickup, P. G. Recent Advances in Direct Formic Acid Fuel Cells (DFAFC). *J. Power Sources* **2008**, *182*, 124−132.
(2) Wang, X.; Hu, J. M.; Hsing, I. M. Electrochemical Investigation of Formic Acid Electro-oxidation and its Crossover through a Nafion Membrane. *J. Electroanal. Chem.* **2004**, *562*, 73−80.
(3) Rice, C.; Ha, S.; Masel, R. I.; Wieckowski, A. Catalysts for Direct Formic Acid Fuel Cells. *J. Power Sources* **2003**, *115*, 229−235.
(4) Rice, C.; Ha, S.; Masel, R. I.; Waszczuk, P.; Wieckowski, A.; Barnard, T. Direct Formic Acid Fuel Cells. *J. Power Sources* **2002**, *111*, 83−89.

DOI: 10.1021/acsami.5b01848
ACS Appl. Mater. Interfaces 2015, 7, 15223−15229

(5) Chen, W.; Chen, S. Iridium-platinum Alloy Nanoparticles: Composition-Dependent Electrocatalytic Activity for Formic Acid Oxidation. *J. Mater. Chem.* **2011**, *21*, 9169−9178.
(6) Chen, W.; Kim, J.; Sun, S.; Chen, S. Composition Effects of FePt Alloy Nanoparticles on the Electro-Oxidation of Formic Acid. *Langmuir* **2007**, *23*, 11303−11310.
(7) Capon, A.; Parsons, R. The Oxidation of Formic Acid at Noble Metal Electrodes Part III. Intermediates and Mechanism on Platinum Electrodes. *J. Electroanal. Chem. Interfacial Electrochem.* **1973**, *45*, 205−231.
(8) Capon, A.; Parsons, R. The Oxidation of Formic Acid on Noble Metal Electrodes: II. A Comparison of the Behaviour of Pure Electrodes. *J. Electroanal. Chem. Interfacial Electrochem.* **1973**, *44*, 239−254.
(9) Igarashi, H.; Fujino, T.; Zhu, Y.; Uchida, H.; Watanabe, M. CO Tolerance of Pt Alloy Electrocatalysts for Polymer Electrolyte Fuel Cells and the Detoxification Mechanism. *Phys. Chem. Chem. Phys.* **2001**, *3*, 306−314.
(10) Jiang, J.; Kucernak, A. Mesoporous Microspheres Composed of PtRu Alloy. *J. Electroanal. Chem.* **2002**, *520*, 64−70.
(11) Lović, J. D.; Tripković, A. V.; Gojković, S. L.; Popović, K. D.; Tripković, D. V.; Olszewski, P.; Kowal, A. Kinetic Study of Formic Acid Oxidation on Carbon-Supported Platinum Electrocatalyst. *J. Electroanal. Chem.* **2005**, *581*, 294−302.
(12) Sun, S. G.; Clavilier, J.; Bewick, A. The Mechanism of Electrocatalytic Oxidation of Formic Acid on Pt (100) and Pt (111) in Sulphuric Acid Solution: An Emirs Study. *J. Electroanal. Chem. Interfacial Electrochem.* **1988**, *240*, 147−159.
(13) Zhang, Z.; More, K. L.; Sun, K.; Wu, Z.; Li, W. Preparation and Characterization of PtFe Nanoleaves as Electrocatalysts for Oxygen Reduction Reaction. *Chem. Mater.* **2011**, *23*, 1570−1577.
(14) Arenz, M.; Stamenkovic, V.; Schmidt, T. J.; Wandelt, K.; Ross, P. N.; Markovic, N. M. The Electro-Oxidation of Formic Acid on Pt-Pd Single Crystal Bimetallic Surfaces. *Phys. Chem. Chem. Phys.* **2003**, *5*, 4242−4251.
(15) Yang, J.; Tian, C.; Wang, L.; Fu, H. An Effective Strategy for Small-Sized and Highly-Dispersed Palladium Nanoparticles Supported on Graphene with Excellent Performance for Formic Acid Oxidation. *J. Mater. Chem.* **2011**, *21*, 3384−3390.
(16) Wang, J. Y.; Kang, Y. Y.; Yang, H.; Cai, W. B. Boron-Doped Palladium Nanoparticles on Carbon Black as a Superior Catalyst for Formic Acid Electro-oxidation. *J. Phys. Chem. C* **2009**, *113*, 8366−8372.
(17) Jung, W. S.; Han, J.; Ha, S. Analysis of Palladium-based Anode Electrode Using Electrochemical Impedance Spectra in Direct Formic Acid Fuel Cells. *J. Power Sources* **2007**, *173*, 53−59.
(18) Miyake, H.; Okada, T.; Samjeské, G.; Osawa, M. Formic Acid Electrooxidation on Pd in Acidic Solutions Studied by Surface-enhanced Infrared Absorption Spectroscopy. *Phys. Chem. Chem. Phys.* **2008**, *10*, 3662−3669.
(19) Zhang, L.; Tang, Y.; Bao, J.; Lu, T.; Li, C. A Carbon-Supported Pd-P Catalyst as the Anodic Catalyst in a Direct Formic Acid Fuel Cell. *J. Power Sources* **2006**, *162*, 177−179.
(20) Li, R.; Hao, H.; Cai, W. B.; Huang, T.; Yu, A. Preparation of Carbon Supported Pd-Pb Hollow Nanospheres and Their Electrocatalytic Activities for Formic Acid Oxidation. *Electrochem. Commun.* **2010**, *12*, 901−904.
(21) Koper, M. T. M.; Lukkien, J. J.; Jansen, A. P. J.; van Santen, R. A. Lattice Gas Model for CO Electrooxidation on Pt-Ru Bimetallic Surfaces. *J. Phys. Chem. B* **1999**, *103*, 5522−5529.
(22) Iwasita, T. Electrocatalysis of Methanol Oxidation. *Electrochim. Acta* **2002**, *47*, 3663−3674.
(23) Wang, X.; Tang, Y.; Gao, Y.; Lu, T. Carbon-Supported Pd-Ir Catalyst as Anodic Catalyst in Direct Formic Acid Fuel Cell. *J. Power Sources* **2008**, *175*, 784−788.
(24) Aramata, A.; Yamazaki, T.; Kunimatsu, K.; Enyo, M. Electrooxidation of Methanol on Iridium in Acidic Solutions: Electrocatalysis and Surface Characterization by Infrared Spectroscopy. *J. Phys. Chem.* **1987**, *91*, 2309−2314.
(25) Shen, S. Y.; Zhao, T. S.; Xu, J. B. Carbon-Supported Bimetallic PdIr Catalysts for Ethanol Oxidation in Alkaline Media. *Electrochim. Acta* **2010**, *55*, 9179−9184.
(26) Assumpcao, M. H. M. T.; da Silva, S. G.; De Souza, R. F. B.; Buzzo, G. S.; Spinace, E. V.; Santos, M. C.; Neto, A. O.; Silva, J. C. M. Investigation of PdIr/C Electrocatalysts as Anode on the Performance of Direct Ammonia Fuel Cell. *J. Power Sources* **2014**, *268*, 129−136.
(27) Zhou, W. J.; Lee, J. Y. Carbon-Supported Pd-Pt Nanoalloy with Low Pt Content and Superior Catalysis for Formic Acid Electro-oxidation. *J. Phys. Chem. C* **2008**, *112*, 3789−3793.
(28) Zhou, W. P.; Lewera, A.; Larsen, R.; Masel, R. I.; Bagus, P. S.; Wieckowski, A. Size Effects in Electronic and Catalytic Properties of Unsupported Palladium Nanoparticles in Electrooxidation of Formic Acid. *J. Phys. Chem. B* **2006**, *110*, 13393−13398.
(29) Xu, C.; Liu, Y.; Wang, J.; Geng, H.; Qiu, H. Nanoporous PdCu Alloy for Formic Acid Electro-oxidation. *J. Power Sources* **2012**, *199*, 124−131.
(30) Lu, Y.; Chen, W. One-pot Synthesis of Heterostructured Pt-Ru Nanocrystals for Catalytic Formic Acid Oxidation. *Chem. Commun.* **2011**, *47*, 2541−2543.
(31) Ioroi, T.; Yasuda, K. Platinum-Iridium Alloys as Oxygen Reduction Electrocatalysts for Polymer Electrolyte Fuel Cells. *J. Electrochem. Soc.* **2005**, *152*, A1917−A1924.
(32) Radmilovic, V.; Gasteiger, H. A.; Ross, P. N. Structure and Chemical Composition of a Supported Pt-Ru Electrocatalyst for Methanol Oxidation. *J. Catal.* **1995**, *154*, 98−106.
(33) Huang, H.; Wang, X. Pd Nanoparticles Supported on Low-defect Graphene Sheets: For Use as High-performance Electrocatalysts for Formic Acid and Methanol Oxidation. *J. Mater. Chem.* **2012**, *22*, 22533−22541.
(34) Meng, H.; Sun, S.; Masse, J. P.; Dodelet, J. P. Electrosynthesis of Pd Single-Crystal Nanothorns and Their Application in the Oxidation of Formic Acid. *Chem. Mater.* **2008**, *20*, 6998−7002.
(35) Chen, W.; Kim, J.; Sun, S.; Chen, S. Electro-oxidation of Formic Acid Catalyzed by FePt Nanoparticles. *Phys. Chem. Chem. Phys.* **2006**, *8*, 2779−2786.
(36) Dinh, H. N.; Ren, X.; Garzon, F. H.; Piotr, Z.; Gottesfeld, S. A Pt-Ru/Graphitic Carbon Nanofiber Nanocomposite Exhibiting High Relative Performance as a Direct-Methanol Fuel Cell Anode Catalyst. *J. Electroanal. Chem.* **2000**, *491*, 222−233.
(37) Liu, Z.; Zhang, X. Carbon-Supported PdSn Nanoparticles as Catalysts for Formic Acid Oxidation. *Electrochem. Commun.* **2009**, *11*, 1667−1670.
(38) Hu, S.; Scudiero, L.; Ha, S. Electronic Effect on Oxidation of Formic Acid on Supported Pd-Cu Bimetallic Surface. *Electrochim. Acta* **2012**, *83*, 354−358.
(39) Lee, S.; Jung, N.; Cho, J.; Park, H.; Ryu, J.; Jang, I.; Kim, H.; Cho, E.; Park, Y.; Ham, H. C.; Jang, J. H.; Yoo, S. J. Surface-Rearranged Pd_3Au/C Nanocatalysts by Using CO-Induced Segregation for Formic Acid Oxidation Reactions. *ACS Catal.* **2014**, *4*, 2402−2408.
(40) Mazumder, V.; Chi, M.; Mankin, M. N.; Liu, Y.; Metin, O.; Sun, D.; More, K. L.; Sun, S. A Facile Synthesis of MPd (M = Co, Cu) Nanoparticles and Their Catalysis for Formic Acid Oxidation. *Nano Lett.* **2012**, *12*, 1102−1106.
(41) Lu, Y.; Chen, W. PdAg Alloy Nanowires: Facile One-Step Synthesis and High Electrocatalytic Activity for Formic Acid Oxidation. *ACS Catal.* **2012**, *2*, 84−90.
(42) Liu, H. X.; Tian, N.; Brandon, M. P.; Pei, J.; Huangfu, Z. C.; Zhan, C.; Zhou, Z. Y.; Hardacre, C.; Lin, W. F.; Sun, S. G. Enhancing the Activity and Tuning the Mechanism of Formic Acid Oxidation at Tetrahexahedral Pt Nanocrystals by Au Decoration. *Phys. Chem. Chem. Phys.* **2012**, *14*, 16415−16423.
(43) Neurock, M.; Janik, M.; Wieckowski, A. A First Principles Comparison of the Mechanism and Site Requirements for the Electrocatalytic Oxidation of Methanol and Formic Acid over Pt. *Faraday Discuss.* **2009**, *140*, 363−378.

DOI: 10.1021/acsami.5b01848
ACS Appl. Mater. Interfaces 2015, 7, 15223−15229